

Near-Infrared Heterojunction Field Modulated Phototransistors with Distinct Photodetection/Photostorage Switching Feature for Artificial Visuals

Jun Wang (✉ uestc_wj@yahoo.com)

School of Optoelectronic Science and Engineering, University of Electronic Science and Technology of China <https://orcid.org/0000-0003-2370-2964>

Xiaoyang Du

School of Optoelectronic Science and Engineering, University of Electronic Science and Technology of China

Jiayue Han

School of Optoelectronic Science and Engineering, University of Electronic Science and Technology of China

Zhengan Zhang

State Key Laboratory of Infrared Physics, Shanghai Institute of Technical Physics, Chinese Academy of Science

Zeyu He

School of Optoelectronic Science and Engineering, University of Electronic Science and Technology of China

RunZhang Xie

Shanghai Institute of Technical Physics, Chinese Academy of Sciences

Chong-Xin Shan

Henan Key Laboratory of Diamond Optoelectronic Materials and Devices, School of Physics and Engineering, Zhengzhou University

Silu Tao

School of Optoelectronic Science and Engineering, University of Electronic Science and Technology of China

Weida Hu

Shanghai Institute of Technical Physics, Chinese Academy of Sciences <https://orcid.org/0000-0001-5278-8969>

Yang Ming

School of Optoelectronic Science and Engineering, University of Electronic Science and Technology of China

Jun Gou

School of Optoelectronic Science and Engineering, University of Electronic Science and Technology of China

Zhiming Wu

School of Optoelectronic Science and Engineering, University of Electronic Science and Technology of China

Yadong Jiang

School of Optoelectronic Science and Engineering, University of Electronic Science and Technology of China

Article

Keywords: Phototransistors, near-infrared imaging, graphene/organic heterojunction, photodetection/photostorage switching, artificial visual

Posted Date: February 25th, 2021

DOI: <https://doi.org/10.21203/rs.3.rs-129595/v1>

License:  This work is licensed under a Creative Commons Attribution 4.0 International License.

[Read Full License](#)

Near-Infrared Heterojunction Field Modulated Phototransistors with Distinct Photodetection/Photostorage Switching Feature for Artificial Visuals

Jiayue Han,^{1,†} Xiaoyang Du,^{1,†} Zhenghan Zhang,^{2,3,†} Zeyu He,¹ Runzhang Xie,³ Chongxin Shan,⁴ Silu Tao,^{1,} Weida Hu,^{3,*} Ming Yang,¹ Jun Gou,^{1,5} Zhiming Wu,^{1,5} Yadong Jiang^{1,5} and Jun Wang^{1,5,*}*

1.School of Optoelectronic Science and Engineering, University of Electronic Science and Technology of China, Chengdu 610054, China

2.State Key Laboratory of ASIC and System, School of Microelectronics, Fudan University, Shanghai, China.

3.State Key Laboratory of Infrared Physics, Shanghai Institute of Technical Physics, Chinese Academy of Science, 500 Yutian Road, Shanghai 200083, China

4.Henan Key Laboratory of Diamond Optoelectronic Materials and Devices, School of Physics and Engineering, Zhengzhou University, Zhengzhou 450001, China

Prof. J. Gou, Prof. Z. Wu, Prof. Y. Jiang, Prof. J. Wang

5.State Key Laboratory of Electronic Thin Films and Integrated Devices, University of Electronic Science and Technology of China, Chengdu 610054, China

† These authors contributed equally to this work.

*Silu Tao: E-mail: silutao@uestc.edu.cn

*Weida Hu: E-mail: wdhu@mail.sitp.ac.cn

*Jun Wang: E-mail: wjun@uestc.edu.cn

Key words:

Phototransistors, near-infrared imaging, graphene/organic heterojunction, photodetection/photostorage switching, artificial visual

Abstract

With the rising demand of recording, computing and image capture, advanced optoelectronic detection, storage and logic devices are highly pursued. Nevertheless, multi-functional vision chip based on infrared detection and memory switching has never been demonstrated. Here, by utilizing the electronic extraction layer ZnO and face-on orientation of D-A, we exhibit the broadband visible to near-infrared photo-response and photo-storage characters on graphene phototransistor. Functions as photodetection and photo-storage can be switched with the variation of gate voltage. The device demonstrates high photo-responsivity up to 1.88×10^6 A/W at 895 nm corresponding detectivity of 4.8×10^{12} Jones. Importantly, the rewritable and switching infrared optoelectronic memory function can be achieved with good retention over 10^4 s. The both retinomorphic vision and memorial preprocessing in artificial visual are simultaneously realized by photodetection/photostorage switching property. Such nearly all-solution processes in our phototransistors may open up the path for the large-scale and easy manufacturing infrared multifunctional bio-optoelectronic device.

Main text

The exotic optoelectronic and quantum properties, such as ultrahigh mobility, tunable Fermi level, superconductivity feature and modified electronic spectra, are explored in graphene system.¹⁻³ To probe all these phenomena, graphene field-effect transistor framework offers the vital platform for devising multi-functional optoelectronic devices.⁴ For the limitation of broadband absorption in monolayer graphene (2.3%), researches initially integrate graphene with single component semiconductor for high performance phototransistors utilizing photo-gating effect.⁵⁻¹³ Nevertheless, most of photoconductive gating devices suffer low operation time (typically millisecond) due to the prolonged life time of carriers.^{14,15} In addition, thick light-harvesting layer may promote the absorption proportion but suffer inferior transfer efficiency due to restriction of nanometer range in effective exciton length.¹⁶ To settle this trade-off relations, ultra-thin light-harvesting layer and valid intrinsic dissociation electric field are needed.¹⁷ Therefore, the ultra-thin type-II Donor-Acceptor (D-A) heterojunctions, such as PCBM/perovskite,¹⁸ PTCDA/pentacene¹⁹ and C₆₀/pentacene,²⁰ are proposed onto graphene for improving the quantum efficiency (QE) up to around 10% compared with the single component enhanced devices. Since the absent of blocking layer may cause recombination energy losses in graphene/Acceptor interface and molecular packing orientation for efficient charge transfer, suggesting that there is still space to improve.

As we enter the areas like big data and cloud computing, more compatibility and complexity memory cells are urgently needed to exploit.²¹⁻²³ With the emerge of technique in 2D materials, the high performance three-terminal semi-floating gate, floating gate and two-terminal ferroelectric tunnel junction memory structures are manufactured without dangling bonds.²⁴⁻²⁷ And optoelectronic memory promotes the data transport without limitation of short interconnections. Nevertheless, infrared optoelectronic memory has acquired far less attention, which is vital for image capture and optical communication.^{28,29} Infrared optical communication requires fast optoelectronic conversion-relaxation,³⁰ photo-storage³¹ and logical operation³². Especially, the

multi-functional high performance optoelectronic devices are highly pursued, where the image sensing and processing functions in separated vision chips can integrate together for promoting the efficiency of vision system.

Here, by utilizing electronic extraction layer ZnO and face-on orientation of D-A molecular packing into D-A/graphene system, we explore the graphene/ZnO/PTB7-Th:IEICO-4F bulk heterojunction (BHJ) field-effect transistor with prominent infrared broadband photo-response (488-1064 nm) and photo-storage phenomena. We can operate both photo-response and photo-storage in one device simultaneously. And four optoelectronic states can be switched by gate voltage. The electronic extraction and deep hole trapping state provided by ZnO, remarkably promote the speed of photo-generated electrons into channel with fastest 178 μ s. while the ZnO layer prevents the holes from graphene injection into D-A hybrid with recombination energy losses, resulting in high EQE up to 2.6×10^8 %. Rely on the conspicuous infrared absorption of PTB7-Th:IEICO-4F heterojunction and novel structure, we perform a high detectivity of 4.8×10^{12} Jones at 895 nm and photo-responsivity up to 1.88×10^6 A/W. Furthermore, we find that deep P-type graphene controlled by gate (operated at -30 V) with appropriate input light power can achieve good retention (over 10^4 s) infrared photo-storage. The gate-tunable rewritable and infrared optoelectronic switching features suggest that phototransistor can be applied to retinomorph vision and memorial preprocessing in artificial visual. The infrared responsivity and memory dual functional device paves the new path for fabricating non-floating gate advanced neural network phototransistor in future.

Results and discussions

The CVD mono-layer graphene was transferred onto the SiO₂/Si⁺⁺ substrate by solution process with prepared bottom gate. After the Au electrode onto the graphene, ZnO and BHJ layer was formed by solution spin-coating method with the thickness of 15 nm and 35 nm (**Fig. 1a**), respectively. ZnO nanoparticle was used as electronic extraction layer for its high electron mobility, matched energy levels with graphene and remarkable environmental stability (**Fig. S1**). PTB7-Th:IEICO-4F was utilized as photosensitive layer, which is due to the broad response wave band (488-1064 nm) as shown in **Fig. S2a**. After spin coating, each component is confirmed by Raman spectroscopy (**Fig. S2b** and more peaks characterization in **Fig. S3**). The D-A hybrid exhibited bi-continuous interpenetrating network structure with appropriate phase separation size (**Fig. S2c**), which is beneficial for exciton dissociation and charge transport. Meanwhile, the unique BHJ morphology allows the phototransistor with thicker photosensitive layer than traditional plane structure, and then guarantee a high response current. AFM image of the BHJ layer showed smooth film surface with a small root-mean-square (RMS) roughness of 2.65 nm (**Fig. S2d**), implied satisfactory interfacial contact between BHJ and ZnO layers. Moreover, demonstrated via Grazing-incidence wide-angle X-ray scattering (GIWAXS) measurement in **Fig. S2e**, the combination of PTB7-Th and IEICO-4F displayed ordered and compact molecular packing in face-on orientation, which was conducive to achieve efficient charge transport in vertical direction.

Next, we further perform the intrinsic optical responsivity of hybrid phototransistor. Interestingly, we observe the four different optoelectronic switching states with the variation gate (**Fig. 1b** and **Fig. S2f**). When the applied gate voltage is about -20 V, photo-memory behavior predominates in our device (**Fig. 1c**). As the increasing of gate voltage, device switched from photo-

memory state to no-memory response state and off-state (**Fig. 1d** to **f**).

The gate-control graphene device shows an asymmetry bi-polar photocurrents with different input power in **Fig. 2a**, indicating a distinct band alignment and mobility for carriers. With the different wavelengths of light excitation onto the device, all exhibit negative photocurrents from 488 nm to 1064 nm, which are highly reproducible and stable under the V_g of 10 V as plotted in **Fig. S4**. Since the IEICO-4F is a non-fullerene acceptor with the LUMO (HUMO) of 4.16 eV (5.44 eV) and PTB7-Th is a donor with LUMO (HUMO) of 3.55 eV (5.27 eV) for formation of type-II heterojunction for exciton separation and charge transfer.^{33,34} In this configuration, graphene acts as collective channel, PTB7-Th:IEICO-4F bulk heterojunction work as mainly absorption layer in visible-infrared regime (on the basic of the absorption spectra in **Fig. S2a**). However, the carrier mobility of blend structure PTB7-Th:IEICO-4F is relatively low which leads the carrier recombination before collected by graphene channel.³⁵ Thus, we restrict the thickness of active blend heterojunction into 35 nm scale for facilitating the photo-response. The control device without ZnO layer still exhibits inferior performance as shown in **Fig. S5**, suggests that photo-generated holes and electrons recombination in graphene. With the strong electron affinity of ZnO due to energy band alignment, implies the intensive electrons extraction from D-A system PTB7-Th:IEICO-4F to graphene channel (**Fig. 2b**). Under the illumination of light, photo-generated hole-electron pairs dissociated and electrons are extracted into graphene causing a N-doping, leading the negative photocurrents (**Fig. 2c**). The intrinsic graphene is hole dominated characterized by the transfer curve in dark condition with a Dirac point at 27.6 V (**Fig. 2c**). The 5 mW/cm² 895 nm light induced a N-doping negative shift with new Dirac point at 7.2 V, which induce carriers variation can be computed by light-doping expression: $\Delta n = C_{ox}|V_g - V_{Dirac}|/e - \sigma/e\mu$. As the consequence, a concentration of $1.39 \times 10^{12}/\text{cm}^2$ photo-generated electrons transfer into graphene.

To better understand the negative or positive photo-response dynamic, we further investigate the bi-directional time-resolved photocurrents measurements with the variation of V_g in **Fig. S6a** and **3a**. With the V_g growth, the intrinsic negative infrared 940 nm photo-responses significantly converts into positive photocurrents (**Fig. S6a**). When ($V_g < V_{Dirac}=27.6$ V), the hole predominates in graphene channel (**Fig. 2b** and **c**). The photo-generated electrons inject into graphene, giving a negative response (**Fig. S6a** top panel). And at deep-hole condition (such as $V_g=-13$ V), the bending energy band can remarkably promote the electrons injection with direct photocurrent of 3.23-fold improvement compared to $V_g=10$ V (**Fig. 2c**). In the electron branch with V_g increasing ($V_g > V_{Dirac}=27.6$ V), we observe the positive photocurrents with increasing and degradation which is slightly distinct with hole branch. The main reason accounts for this inhibition photocurrents when $V_g > 40$ V is that the Fermi level of electron-dominated graphene may approaches or exceed LUMO level of ZnO (4.4 eV), causing the carrier quenching. For further acquisition of optimized photo-responsivity, we characterize the photocurrent as the function of V_g sweeping from -20 V to 65 V with the variation of input optical power density (**Fig. 2a**). The asymmetry bidirectional photocurrents imply that deep-hole graphene can induce the higher photo-gating effect at sacrifice of the response time (**Fig. 1c** and **d**). And positive responses start degradation when the V_g exceeding 42.8 V (the corresponding work function is nearly 4.43 eV which can be determined by $E_f = h$

$v_F \sqrt{\pi C_{ox}|V_g - V_{Dirac}|/e}$).³⁶ As we can see in **Fig. 2c**, the transfer curves under the irradiation of light show a bending near the V_g approaches 40 V, revealing validity of the photocurrents inhibition

theory proposed before. Moreover, our graphene heterojunction photoconductor exhibits linear photocurrent with bias voltage at various V_g (**Fig. S6b**).

When the V_g approaches 7.5 V (hole branch of graphene), the device shows no photo-memory due to the shallow trapping state for electron. By utilizing the gate modulation tendency from **Fig. 2a**, we present the detailed no memory optimized photo-responsivity (R) measurements with the constant $V_g=10$ V and $V_g=50$ V. The power-dependent time-resolved responses are measured in **Fig. 2d**, demonstrating the prominent photo-sensitive capacity even at ultra-low input optical power (895 nm, 14.4 nW/cm², $V_g=10$ V and 50 V). And the highest infrared R of 1.88×10^6 A/W in negative responses and 1.3×10^6 A/W at positive responses, which is comparable with infrared detection performance of graphene based phototransistors.^{10,37} The **Fig. 2e** shows a logarithm linear relation in most excitation wavelength and R decreases with the light irradiation with the variation tendency: $R = \frac{\alpha C_i \mu V_{ds}}{WL} p^{\beta-1}$, Especially for the 895nm photo-responses as illustrated inset the **Fig.**

2e, the fitting curve show linear photo-gating hole trapping state with the $\beta = 0.417$. whereas for 1064 nm, the linear relation of R -Power shows a saturation around 1.16 μ W/cm² and the (**Fig. 2e**) corresponding to the cut-off edge of D-A absorption around 1 μ m. Compared with previous bilayer and bulk heterojunction enhanced graphene, our device exhibits nearly 2 to 100 fold improvement in R .¹⁸⁻²⁰

In sensitized photo-gating phototransistors, the prolonged recombination time of trapping carriers and another type of carriers recycled in channel, yielding high gain responses. Therefore, the gain (recycled times) is associated with recombination time and computed by $G = \frac{\tau_{life}}{\tau_{transit}}$, where the τ_{life} is the life time of carriers and the $\tau_{transit}$ is the transit can be estimated by $\tau_{transit} = l^2 / \mu V_{ds}$ (the μ is obtain by **Fig. S7**). The relative long recovery time always originates inferior operation time of device. Consequently, there is a trade-off relation between the R and operation bandwidth. The transient responses of device with different gate biases are measured in **Fig. S8a**. The response and recover time are respectively 178 μ s and 1.41 ms at V_{ds} of 1 V with 15 V V_g (**Fig. S8a** top panel), which is superior with the majority of previous graphene photoconductive works.^[5-12,17-20] For higher responsivity, the recovery time has been prolonged to 32 ms at 10 V V_g (**Fig. S8a** bottom panel). Thus, the gain of negative infrared responses reaches up to 5.01×10^6 with EQE up to 2.6×10^8 % under 10 V V_g .

To further investigate the signal-noise character of negative infrared responses, we perform gate-dependent noise spectral in **Fig. S8b**. At the $V_g=20$ V, the noise spectral density can reach lowest at 1.23×10^{-9} (100 Hz) due to direct suppression of dark current near the Dirac point. We use a simple but precise method to evaluate the detectivity by formula: $D^* = R(Sf)^{\frac{1}{2}} I_n^{-1}$,³⁸ where the f represents operation frequency, S stands for active area and I_n is the noise current. With the measured noise characterization (**Fig. S8b**) and responsivity-frequency relation (**Fig. S9**), the color map of detectivity (D^*) can be plotted as depicted in **Fig. 2f**. At the bias of 1 V, the values of D^* in low frequency regime (1-10 Hz) fluctuates from 10^{10} - 10^{12} Jones due to the affection of flicker noise. When the f approaches the bandwidth (127 Hz) of device, the D^* shows over 1.4×10^{12} Jones mainly in region of infrared band (780-940 nm). The maximum of D^* can be achieved up to 4.8×10^{12} Jones at frequency of 100 Hz with the applied gate 10 V.

After systematic investigation on crucial parameters of no-memory photo-response, the long-

term infrared photo-memory characters are exhibited in deep-hole branch graphene condition. We first carefully explore the infrared photo-induced memory case, **Fig. 3a** depicts the stable and erasable near-infrared storage in 3 cycles when graphene is heavily hole-doped (V_g work at -30 V). We find that the hysteresis phenomenon appears in variation of I_{ds} with V_g relation in **Fig. 3b**. Owing to the prolonged hole trapping state induced by ZnO, the optoelectronic memory function can be tuned and erased by V_g . There is also a conspicuous reference erasing V_g voltage which, as in bending point of transfer curve (arrow in **Fig. 3b**), are implied so as to ensure the value of V_g pulse is adequate for the entirely resettable. The low erasing V_g pulse proved unequal to the reset task (**Fig. S10a**). When the Fermi level of graphene approaches or surpasses the LUMO level of ZnO, corresponding V_g transforms graphene into N-doping. And the N-type graphene can supply abundant electrons into active layer to neutralize hole trapping near ZnO interface for erasing. Therefore, by applying a +60 V V_g pulse, we can rapidly erase the memorial photo-response and reset in nearly 5 seconds (**Fig. 3a**). Note that fast downward pulse in **Fig. 3a**, which is ascribed to transient resistance change of graphene due to V_g pulse.

By utilizing the bi-directional photocurrents switching feature (**Fig. 2a** and **Fig. 3b**), there implies a threshold voltage (V_T) that can modulate the on-off state in photo-induced storage. V_T can be obtained from transfer curve at the node of dark I_{ds} and light I_{ds} branches, which is 13.7 V. The distinct color traces in **Fig. 3c** represent different V_g working state. At the programming occasion (**Fig. 3c** top panel), the photocurrent comes to nearly 574 μA with 151 μA memory current ($V_g = -10$ V) The deep P-doping graphene facilitates the photo-generated electrons injection into graphene giving a strongly memorial response. With V_g approaching the V_T , few of photo-generated electrons neutralize hole in graphene and corresponding holes trapping into active layer resulting in inferior photo-storage or no-memory photo-response condition. However, the practical measurements show that V_T is roughly 20 V due to electric drift effect (**Fig. 3c**). As the V_g reaches 10 V, the photocurrent has slumped to around 99 μA with the no photo-memory. Higher V_g (20 V) attempt to further inhibition of response is plotted in **Fig. 3c** (blue point), the suppression ratio has increased by 95.3 % in terms of $V_g = -10$ V.

More measurements are raised on optimized factors for implement of long-term memory. The pulsed illumination of constant input power at 940 nm with 3 cycles in **Fig. 3d** shows an on-off state at the higher V_g which is ascribed to the different value of Dirac shift induced by 940 nm. The shallow-hole graphene ($V_g = 10, 20$ V) implies obvious relaxation (over 25 % of current losses in 20 s). Furthermore, the power-dependent 'light write-reset' cycles are depicted in **Fig. 3e**. We notice that for stronger input light power (input light $> 12.5 \mu W/cm^2$, light pulse width = 0.5 s), the retention current after light pulse can hardly maintain but quick release to recover, the photocurrent of 91 $\mu W/cm^2$ and 12.5 $\mu W/cm^2$ input light has fallen to 85.4 % and 89.9 % respectively within nearly 20 s. The releasing current fluctuation stay close to the 3.3 % in the same time range under the 1.3 $\mu W/cm^2$ power. And even retention current becomes nearly constant (0.27 % fluctuation) at the power of 0.32 $\mu W/cm^2$. The lower Fermi level of graphene gains much photo-generated electrons traction into channel for larger photocurrents, which may make more contribution to prolong the retention time. **Fig. 3f** shows the deep-hole V_g can promote the retention time limited extent (nearly 2-fold prolong time in **Fig. 3f** top panel and middle panel). And the retention time is also found less correlation with light pulse width (**Fig. S10b**). Thus, we achieve retention time up to 10^4 s with relative small input power (0.32 $\mu W/cm^2$) and deep-hole at higher $V_g = -30$ V (**Fig. 4i** bottom panel).

The exponential fitting of $e^{-\frac{t}{\tau}}$ gives a life time $\tau = 11999$ s with 1 s light pulse (**Fig. 3i** bottom

panel).

Furthermore, we demonstrate 3×4 array for assessment of the infrared imaging performance (**Fig. 4a**). In this test, each detection unit stands for one pixel. The letter “H” pattern is mapping onto the detection array under the 940 nm light irradiation. Two working mode are shown. The receptive field is a part of biological image preprocessing systems, including two types of bipolar cells, on/off cells (When receiving light stimuli, the response of on cells is positive while the response of off cells is negative).³⁹ Our devices function similarly to these cells and can work as a proper simulation of visual processing (**Fig. 4a** and **b**). Based on the device performance, we constructed a 3×3 artificial receptive field, which consists of a central device and 8 surrounding devices. The center device works in the state of negative photocurrent. While the surrounding units work in the state of positive photocurrent. The processing function is demonstrated by the greyscale “Leave” image, shown in **Fig. 4c**, and the process are provided in **Fig. 4b**. Also, by controlling the V_g , more functions were achieved (**Fig. 4b, e** and **f**), which means the reconfigurability of the device array has more potential functions. As an example, two additional functions, embossing, and blur are demonstrated in **Fig. 4e** and **f**. Traditional visual circus processes the image by transporting the image from the camera to the processor, leading to energy waste and efficiency loss on transporting. Different from the traditional visual circus, real-time sensing, and processing greatly avoid the interference of miscellaneous information and improve efficiency. Especially, to deserve to be mentioned that, it is the first time that infrared light was applied in the preprocessing by Van der Waals heterojunctions. Moreover, we mimic memorial preprocessing and forgetting process of human visual systems when the V_g approaches -20 V (**Fig. 4g**). The infrared image memorizations of “H” pattern are shown in **Fig. 4h** with just 1 optical pulse. After the light stimuli, the dimmer “H” pattern is observed with memory effect. By further forgetting process, “H” pattern vanishes. All this processes show the capability of multi-functional infrared artificial visual based on ORRAM array.

This on-off state switching phototransistor demonstrates prominent performance both in photo-storage and photo-detection. The state-of-the-art of sensitized graphene phototransistors with similar framework and photo-memory devices are summarized in **Table 1**. Graphene based photo-conductors have mainly two outlets for high-performance design, like single layer enhanced and bilayer or bulk heterojunction enhanced strategies (**Table 1**). It is notable that the majority devices have averaged over millisecond response time and low photo-responsivity in infrared regime. Our phototransistor exhibits high optical sensitivity in fast response time with simultaneous long-term gate-control photo-memory feature due to high-efficiency multi-layer heterojunction and effective trapping state.

Conclusions

With the system so well-designed, we show a photo-storage and photo-detection switching characteristics in graphene/ZnO/PTB7-Th:IEICO-4F framework phototransistor. The devices show over 10^6 A/W infrared photo-responsivity with fast response time down to 178 μ s and the corresponding D^* is up to 4.8×10^{12} Jones. And a long-term (10^4 s) infrared photo-memory with writing and erasing functions can be achieved. The reset V_g reference value is further validated by bending point of transfer curve. The systematic investigations have been done in tunable infrared photo-memory phenomenon. The infrared retinomorphic vision and memorial preprocessing functions in artificial visual can operate simultaneously. The high performance infrared photo-responses and multi-functional artificial visual applications are highly beneficial for devising future

switching bio-optoelectronic applications with fast speed and high photo-responsivity.

Table 1. Comparison with previous graphene phototransistors and photo-memory device with high performance.

Framework	Active materials	Responsivity [A/W]	Response time [ms]	Spectral range [nm]	Photo-memory Feature	Ref.
Single layer enhance	Graphene/SWNTs	100	0.1	400-1550	NA	10
	Graphene/C ₈ -BTBT	10 ⁴	25	355	NA	17
	Graphene/Rubrene	10 ⁷	100	400-600	NA	13
	Graphene/WS ₂	10 ⁶	0.13	400-700	NA	9
	Graphene/PbS QDS	10 ⁷	10	600-1450	NA	5
	Graphene/MAPbBr ₃	1.4×10 ⁸	4.5×10 ³	430-440	NA	7
	Graphene/COF	3.2×10 ⁷	1.14	400-600	NA	8
Bilayer or Bulk heterojunction enhance	Graphene/PCBM/perovskite	8×10 ⁵	10 ⁶	400-750	NA	18
	Graphene/PTCDA/Pentacene	10 ⁵	0.03	400-700	NA	19
	Graphene/C ₆₀ /Pentacene	9127	0.275	405-1550	NA	20
	Graphene/ZnO/PTB7-Th:IEICO-4F	1.88×10 ⁶	0.178	488-1064	over 10 ⁴ s with switching states	This work
Photo-memory devices	MoS ₂ /PbS	10 ⁷	NA	808-1940	over 10 ⁴ s	31
	ReS ₂ /h-BN/graphene	NA	NA	532	over 10 ⁴ s	32
	Sol-PDI/C ₁₀ -DNNT	NA	NA	405-640	over 10 ⁴ s	40
	diF-TESADT	10 ⁴	NA	575	over 600s	41
	Perovskite/IGZO	10 ⁵	NA	457-1064	over 10 ⁴ s	42
	Graphene/MoS ₂	10 ¹⁰	NA	visible	over 10 ² s	6

Materials and methods

Device Fabrication and Characterization: Single-layer CVD graphene was transferred to an n+ Si/SiO₂ substrate (SiO₂ 285 nm) by a solution method. Then the 90 nm gold electrode is deposited by thermal evaporation with symmetrical contact onto prepared graphene to form a channel (25 μm in length and 250 μm in width). ZnO

precursor solution was formed by dissolving 110 mg of zinc acetate dehydrate ($\text{Zn}(\text{CH}_3\text{COO})_2 \cdot 2\text{H}_2\text{O}$) and 31 mg of ethanolamine in 1 ml of 2-methoxyethanol with stirring overnight, and then was spin-coated on graphene to form 15 nm thin films. PTB7-Th: IEICO-4F (1: 1.5) mixture was dissolved in in CB: CN (96:4, volume ratio) solution with a donor concentration of 8 mg/ml. The thickness of BHJ layer was tuned at 35 nm.

Measurement Methods: The absorption spectra were recorded by Hitachi U-3010 UV-VS. The thickness of BHJ layer was calibrated by a step profilometer (AMBIOS-XP2). Atomic force microscope (AFM, Asylum Research AFM system (MFP-3D-BIO)) and transmission electron microscopy (TEM, Hitachi TEM system) were used to investigate the film morphology. Cross-sectional TEM was acquired using Helios NanoLab 600i. Grazing-incidence wide-angle X-ray scattering (GIWAXS) experiments were performed at BL18U beam line of shanghai synchrotron radiation facility (SSRF) and utilized to analyze the molecule orientation and stacking property of BHJ. All samples were radiated at 12.67 keV X-ray with an incident angle of 0.12° , Pilatus 6M is the detector. All electrical and photo-response characteristics of graphene/organic semiconductor heterojunction phototransistors were measured by a Keithley 2636b source meter analyzer and PDA with different radiation wavelength. Raman spectra measurement was performed by a confocal microprobe Raman spectrometer (RENISHAW inVia Raman Microscope) under the illumination of a 514 nm helium-neon laser.

Acknowledgements

This work was supported in part by the National Natural Science Foundation of China (NSFC Grant No. 61922022, 62075029, 61775029 and 51533005), Royal Society-Newton Advanced Fellowship (Grant No. NA170214), Program of Shanghai Subject Chief Scientist (Grant No.19XD1404100) and the China Postdoctoral Science Foundation (2020TQ0058).

Conflict of interests

The authors declare that they have no conflicts of interest.

Contributions

J.H., X.D., Z.Z. contribute equally to this work. J.W., S.T., W.H. conceived and supervised the project. J.H., X.D. and Z.H. prepared the device and performed the photocurrent measurements and characterizations. J.H. set up the experimental platform, and J.H., X.D., and Z.H. performed the data analysis. Z.Z. performed artificial visual content. J.H., X.D. and Z.Z. co-wrote this paper. All authors discussed the results and commented on the manuscript.

Figure Caption

Fig. 1 | Morphology characterization and multifunctional switching of graphene/organic phototransistor in different V_g . **a**, Cross-sectional TEM image. **b**, Device structure of graphene/ZnO/PTB7-Th:IEICO-4F phototransistor. **c,d,e,f** The time resolved photocurrents under the different V_g . **c**, $V_g=-20$ V, long-term photo-memory state in negative photocurrent. **d**, $V_g=7.5$ V, no memory photo-response state in negative photocurrent. **e**, $V_g=17$ V, off state. **f**, $V_g=40$ V, no memory photo-response state in positive photocurrent.

Fig. 2 | The transfer, no memory photo-responsive characteristics of graphene/organic phototransistor. **a**, V_g and Power dependent photocurrents intensity distribution colormap. **b**, The energy band alignment and charge transfer diagram of the multi-layer heterojunction under the light illumination at different V_g conditions. Top panel is deep-hole graphene circumstance and bottom panel corresponding to shallow-hole or electron branch graphene. **c**, Transfer characteristics of the graphene/organic phototransistor under different input wavelengths with the same power density = 60 mW/cm^2 . **d**, The photocurrent variations of the different V_g values ($V_g=10$ V top panel, $V_g=50$ V bottom panel) with the reductive input light power. **e**, The photo-responsivity plotted as a function of input light power density. The inside is the logarithm linear fitting curve. **f**, The frequency and wavelength dependent color map of detectivity.

Fig. 3 | The transfer, infrared photo-memory cycle and retention characteristics of graphene/organic phototransistor. **a**, The 3 writing and erasing cycles. **b**, The hysteresis transfer curve along with arrow direction and inside is transfer curve of device with or without light illumination. **c**, The gate-dependent photo-memory switching operation. **d**, Gate-related relaxation currents under the constant input light power with 1 s pulse width. For all traces, input light power = $663 \text{ } \mu\text{W/cm}^2$, gate pulse width = 0.25 s. **e**, The 3 programming-relaxation cycle measurements as the function of input light power. light pulse width = 0.5 s, gate pulse width = 0.25 s. **f**, The retention and persistent state of infrared photo-memory with different V_g (two of top panel). Optimized retention in bottom panel with proper input power and V_g .

Fig. 4 | The planar array of graphene/organic phototransistors for reconfigurable retinomorphic vision and memorial preprocessing application. **a**, The schematic diagram of 3×4 array irradiated by infrared light irradiation metal through the shadow mask with 'H' shaped pattern and photoresponse of the negative and positive photoresponsive modes with the infrared 940 nm light (3.76 mW/cm^2) for imaging. Inset is the 3×4 array picture. **b**, Simulations of reconfigurable retinomorphic vision. **c**, Original image. **d**, Edge detection. **e**, Emboss. **f**, Dispose of Blurring. **g**, Schematics of the human visual system. **h**, The illustrations of the image memory of the letter 'H' at memorial preprocessing working mode ($V_g=-20$ V, 940 nm light with 3.76 mW/cm^2 , optical pulse width: 2s, electric pulse width: 1s).

Figures

Fig. 1.

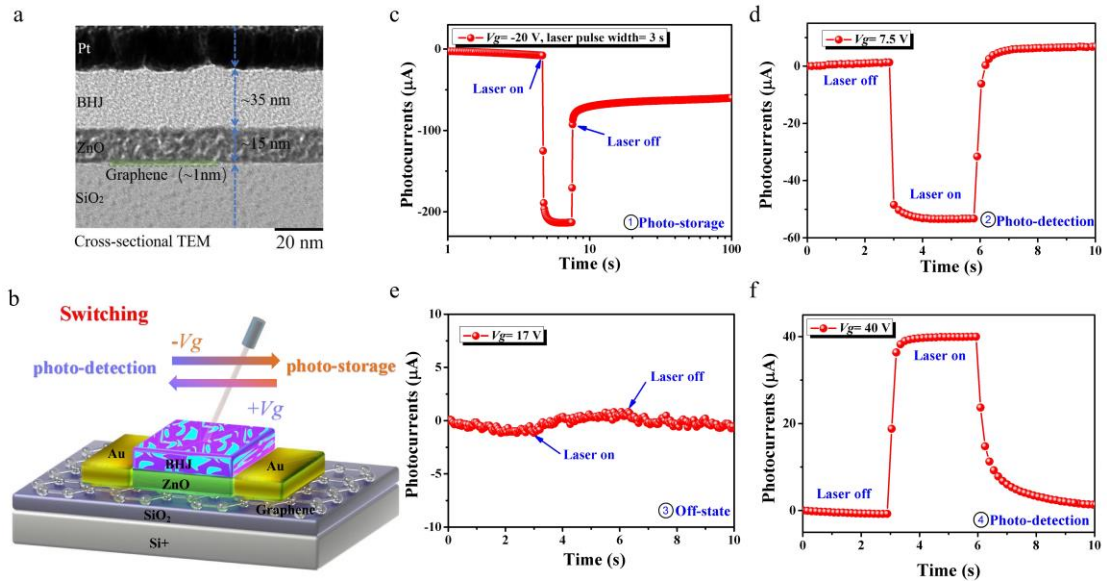


Fig. 2.

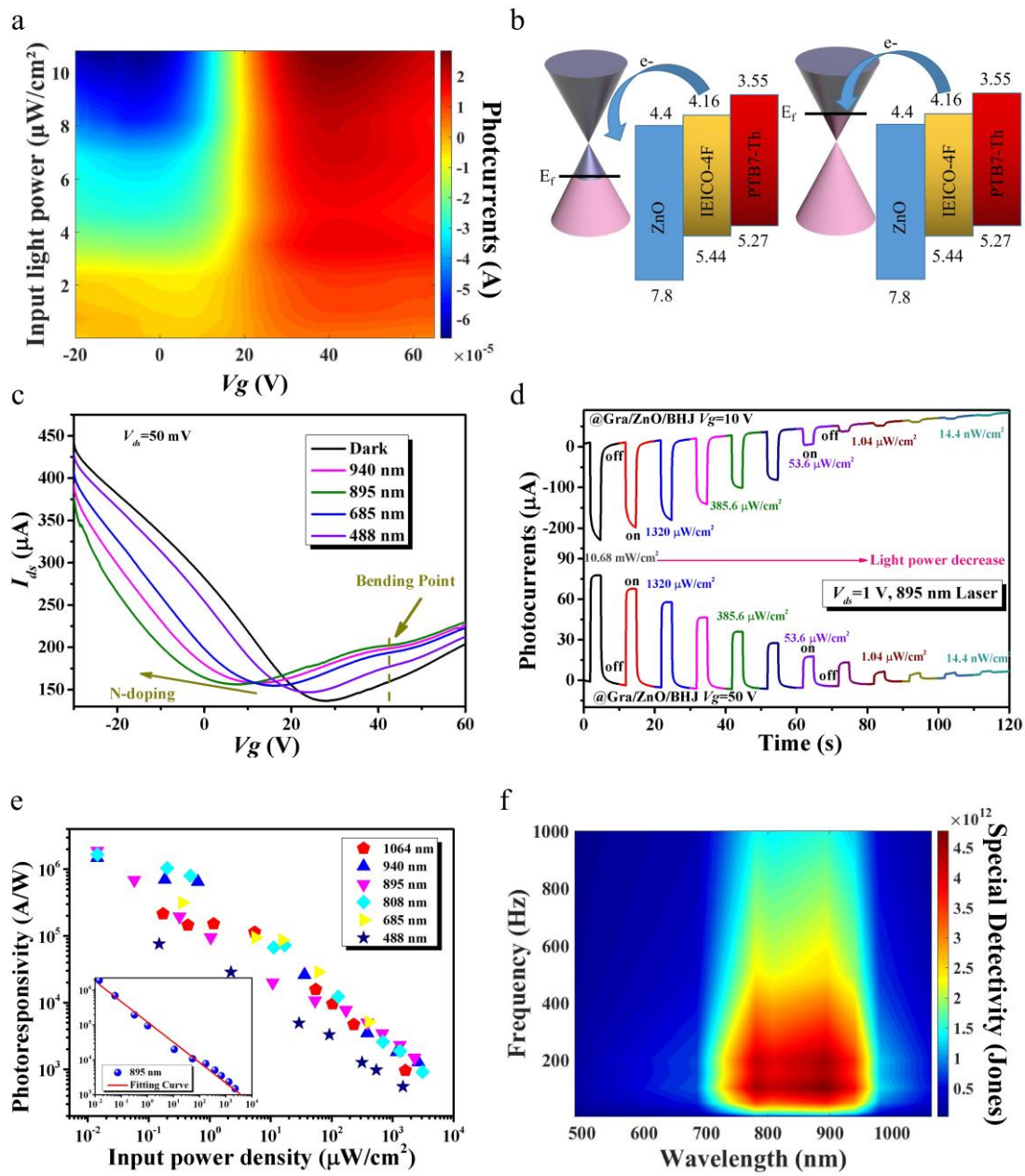


Fig. 3.

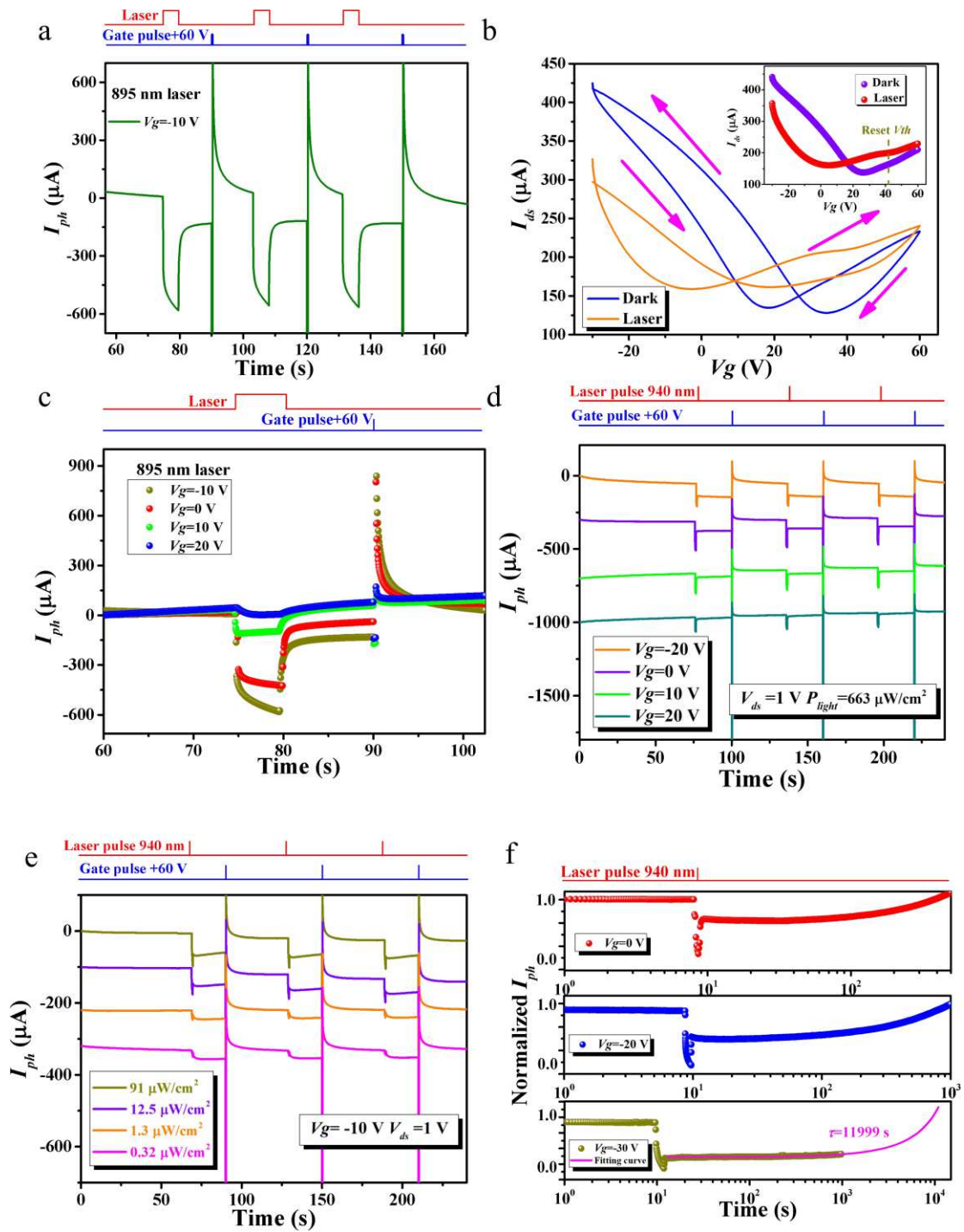
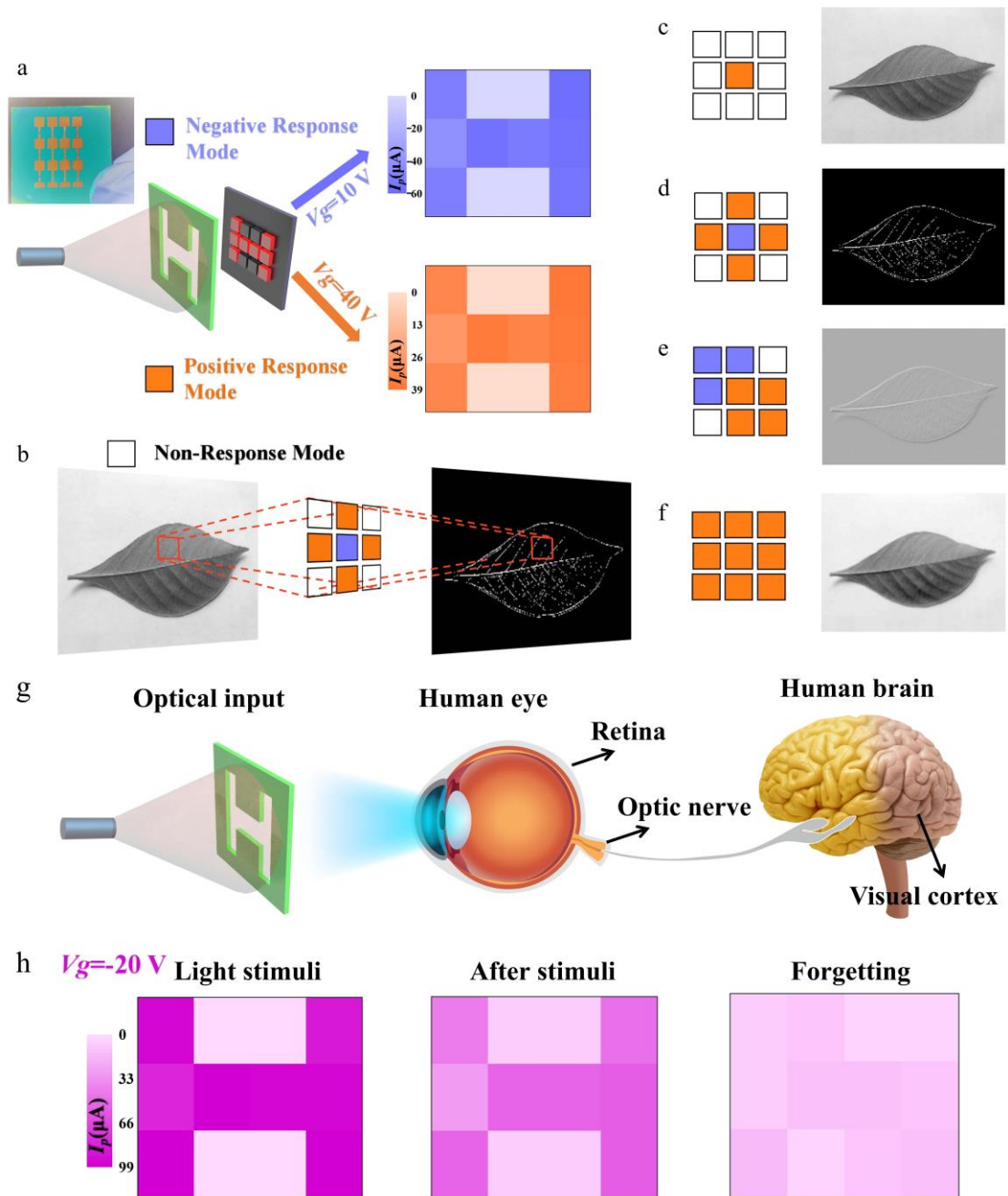


Fig. 4.



Reference

- 1 Nair, R. R. *et al.* Fine structure constant defines visual transparency of graphene. *Science* **320**, 1308-1308, doi:10.1126/science.1156965 (2008).
- 2 Wang, Z. *et al.* Composite super-moire lattices in double-aligned graphene heterostructures. *Science Advances* **5**, doi:10.1126/sciadv.aay8897 (2019).
- 3 Cao, Y. *et al.* Unconventional superconductivity in magic-angle graphene superlattices. *Nature* **556**, 43-+, doi:10.1038/nature26160 (2018).
- 4 Liu, Y. *et al.* Van der Waals heterostructures and devices. *Nature Reviews Materials* **1**, 16042 (2016).
- 5 Konstantatos, G. *et al.* Hybrid graphene-quantum dot phototransistors with ultrahigh gain. *Nature Nanotechnology* **7**, 363-368, doi:10.1038/nnano.2012.60 (2012).
- 6 Roy, K. *et al.* Graphene-MoS₂ hybrid structures for multifunctional photoresponsive memory devices. *Nature Nanotechnology* **8**, 826-830, doi:10.1038/nnano.2013.206 (2013).
- 7 Pradhan, B. *et al.* Ultrasensitive and ultrathin phototransistors and photonic synapses using perovskite quantum dots grown from graphene lattice. *Science Advances* **6**, doi:10.1126/sciadv.aay5225 (2020).
- 8 Xiong, Y. *et al.* Ultrahigh Responsivity Photodetectors of 2D Covalent Organic Frameworks Integrated on Graphene. *Advanced Materials* **32**, 1907242, doi:10.1002/adma.201907242 (2020).
- 9 Mehew, J. D. *et al.* Fast and Highly Sensitive Ionic-Polymer-Gated WS₂-Graphene Photodetectors. *Advanced Materials* **29**, 1700222, doi:10.1002/adma.201700222 (2017).
- 10 Liu, Y. *et al.* Planar carbon nanotube-graphene hybrid films for high-performance broadband photodetectors. *Nature Communications* **6**, 8589, doi:10.1038/ncomms9589 (2015).
- 11 Lee, Y. *et al.* High-Performance Perovskite-Graphene Hybrid Photodetector. *Advanced Materials* **27**, 41-46, doi:10.1002/adma.201402271 (2015).
- 12 Huisman, E. H. *et al.* High Gain Hybrid Graphene-Organic Semiconductor Phototransistors. *Acs Applied Materials & Interfaces* **7**, 11083-11088, doi:10.1021/acsami.5b00610 (2015).
- 13 Jones, G. F. *et al.* Highly Efficient Rubrene-Graphene Charge-Transfer Interfaces as Phototransistors in the Visible Regime. *Advanced Materials* **29**, 1702993, doi:10.1002/adma.201702993 (2017).
- 14 Fang, H. & Hu, W. Photogating in Low Dimensional Photodetectors. *Advanced science* **4**, 1700323, doi:10.1002/advs.201700323 (2017).
- 15 Shin, G. H., Park, C., Lee, K. J., Jin, H. J. & Choi, S.-Y. Ultrasensitive Phototransistor Based on WSe₂-MoS₂ van der Waals Heterojunction. *Nano Letters* **20**, 5741-5748, doi:10.1021/acs.nanolett.0c01460 (2020).
- 16 Baeg, K.-J., Binda, M., Natali, D., Caironi, M. & Noh, Y.-Y. Organic Light Detectors: Photodiodes and Phototransistors. *Advanced Materials* **25**, 4267-4295, doi:10.1002/adma.201204979 (2013).
- 17 Liu, X. *et al.* Epitaxial Ultrathin Organic Crystals on Graphene for High-Efficiency Phototransistors. *Advanced Materials* **28**, 5200-+, doi:10.1002/adma.201600400 (2016).
- 18 Qin, L. *et al.* Using Bulk Heterojunctions and Selective Electron Trapping to Enhance the Responsivity of Perovskite-Graphene Photodetectors. *Advanced Functional Materials* **27**, 1704173, doi:10.1002/adfm.201704173 (2017).
- 19 Chen, X. *et al.* Improving the Performance of Graphene Phototransistors Using a

- Heterostructure as the Light-Absorbing Layer. *Nano Lett* **17**, 6391-6396, doi:10.1021/acs.nanolett.7b03263 (2017).
- 20 Han, J. *et al.* Graphene/Organic Semiconductor Heterojunction Phototransistors with Broadband and Bi-directional Photoresponse. *Adv Mater* **30**, 1804020, doi:10.1002/adma.201804020 (2018).
- 21 Yao, P. *et al.* Fully hardware-implemented memristor convolutional neural network. *Nature* **577**, 641-646, doi:10.1038/s41586-020-1942-4 (2020).
- 22 Zidan, M. A., Strachan, J. P. & Lu, W. D. The future of electronics based on memristive systems. *Nature Electronics* **1**, 22-29, doi:10.1038/s41928-017-0006-8 (2018).
- 23 Liu, C. *et al.* Two-dimensional materials for next-generation computing technologies. *Nature Nanotechnology* **15**, 545-557, doi:10.1038/s41565-020-0724-3 (2020).
- 24 Wu, J. *et al.* High tunnelling electroresistance in a ferroelectric van der Waals heterojunction via giant barrier height modulation. *Nature Electronics* **3**, 466-472, doi:10.1038/s41928-020-0441-9 (2020).
- 25 Yin, L. *et al.* Two-Dimensional Unipolar Memristors with Logic and Memory Functions. *Nano Letters* **20**, 4144-4152, doi:10.1021/acs.nanolett.0c00002 (2020).
- 26 Wang, X. & Wang, J. Ferroelectric tunnel junctions with high tunnelling electroresistance. *Nature Electronics* **3**, 440-441, doi:10.1038/s41928-020-0463-3 (2020).
- 27 Liu, C. *et al.* A semi-floating gate memory based on van der Waals heterostructures for quasi-non-volatile applications. *Nature Nanotechnology* **13**, 404+, doi:10.1038/s41565-018-0102-6 (2018).
- 28 Star, A., Lu, Y., Bradley, K. & Gruner, G. Nanotube optoelectronic memory devices. *Nano Letters* **4**, 1587-1591, doi:10.1021/nl049337f (2004).
- 29 Yin, L. *et al.* Robust trap effect in transition metal dichalcogenides for advanced multifunctional devices. *Nature Communications* **10**, doi:10.1038/s41467-019-12200-x (2019).
- 30 Guo, J. *et al.* High-performance silicon-graphene hybrid plasmonic waveguide photodetectors beyond 1.55 μm . *Light: Science & Applications* **9**, 29, doi:10.1038/s41377-020-0263-6 (2020).
- 31 Wang, Q. *et al.* Nonvolatile infrared memory in MoS₂/PbS van der Waals heterostructures. *Science Advances* **4**, doi:10.1126/sciadv.aap7916 (2018).
- 32 Mukherjee, B. *et al.* Laser-Assisted Multilevel Non-Volatile Memory Device Based on 2D van-der-Waals Few-Layer-ReS₂/h-BN/Graphene Heterostructures. *Advanced Functional Materials*, doi:10.1002/adfm.202001688 (2020).
- 33 Du, X. *et al.* Delayed Fluorescence Emitter Enables Near 17% Efficiency Ternary Organic Solar Cells with Enhanced Storage Stability and Reduced Recombination Energy Loss. *Advanced Functional Materials* **30**, doi:10.1002/adfm.201909837 (2020).
- 34 Shoae, S., Stolterfoht, M. & Neher, D. The Role of Mobility on Charge Generation, Recombination, and Extraction in Polymer-Based Solar Cells. *Advanced Energy Materials* **8**, 1703355, doi:10.1002/aenm.201703355 (2018).
- 35 Jin, Z. *et al.* Improving the photocurrent of a PBDTTT-CF and PCBM based organic thin film photoconductor by forming a bilayer structure. *Rsc Advances* **5**, 84680-84684, doi:10.1039/c5ra16998d (2015).
- 36 Xu, K. *et al.* Direct Measurement of Dirac Point Energy at the Graphene/Oxide Interface. *Nano Letters* **13**, 131-136, doi:10.1021/nl303669w (2013).
- 37 Yu, Y. *et al.* Fast Photoelectric Conversion in the Near-Infrared Enabled by Plasmon-Induced

- Hot-Electron Transfer. *Advanced Materials* **31**, 1903829, doi:10.1002/adma.201903829 (2019).
- 38 Yang, B. *et al.* Bioinspired Multifunctional Organic Transistors Based on Natural Chlorophyll/Organic Semiconductors. *Advanced Materials* **32**, 2001227, doi:10.1002/adma.202001227 (2020).
- 39 Masland, R. H. The fundamental plan of the retina. *Nature Neuroscience* **4**, 877-886, doi:10.1038/nn0901-877 (2001).
- 40 Chiang, Y.-C. *et al.* High-Performance Nonvolatile Organic Photonic Transistor Memory Devices using Conjugated Rod-Coil Materials as a Floating Gate. *Advanced Materials* **32**, doi:10.1002/adma.202002638 (2020).
- 41 Jia, R. *et al.* Unraveling the Mechanism of the Persistent Photoconductivity in Organic Phototransistors. *Advanced Functional Materials* **29**, doi:10.1002/adfm.201905657 (2019).
- 42 Wei, S. *et al.* Flexible Quasi-2D Perovskite/IGZO Phototransistors for Ultrasensitive and Broadband Photodetection. *Advanced Materials* **32**, doi:10.1002/adma.201907527 (2020).

Figures

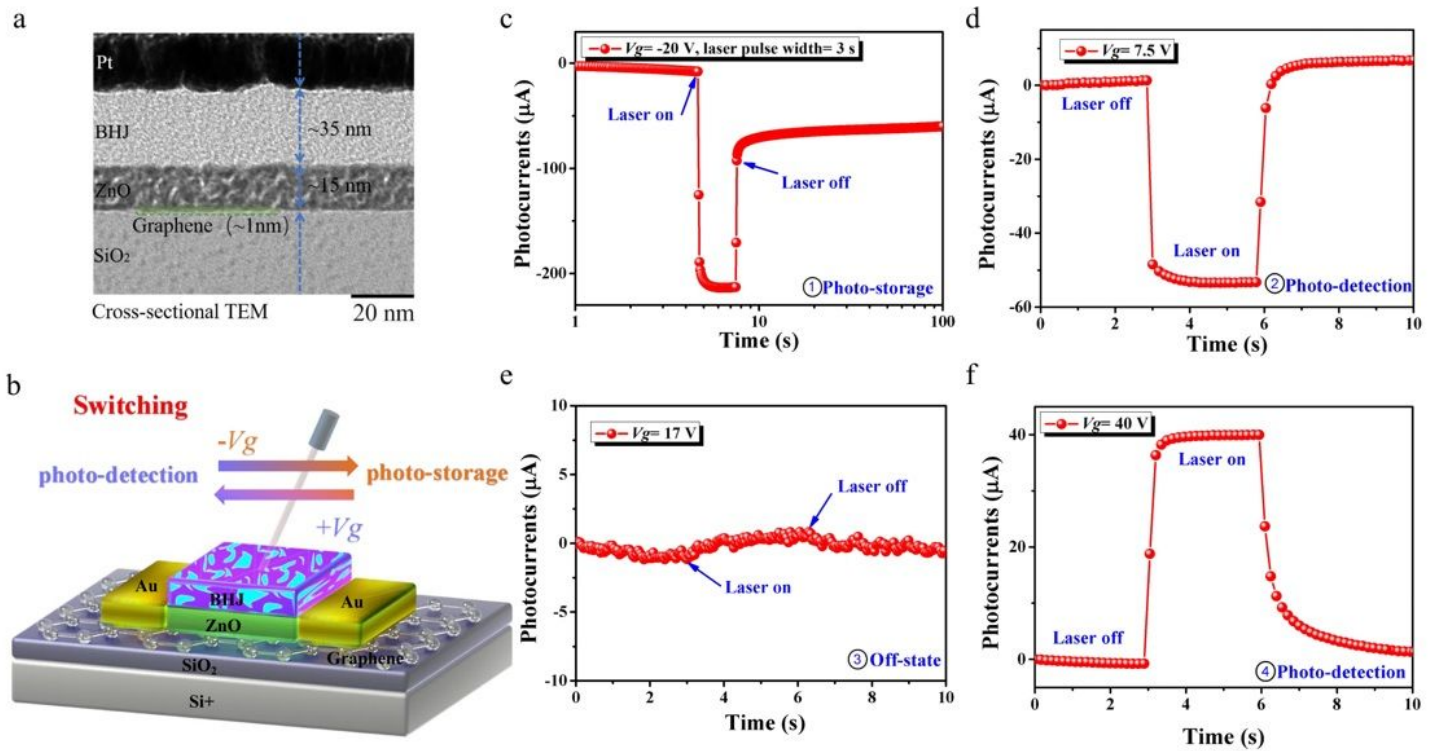


Figure 1

Morphology characterization and multifunctional switching of graphene/organic phototransistor in different V_g . a, Cross-sectional TEM image. b, Device structure of graphene/ZnO/PTB7-Th:IEICO-4F phototransistor. c,d,e,f The time resolved photo-currents under the different V_g . c, $V_g = -20$ V, long-term photo-memory state in negative photocurrent. d, $V_g = 7.5$ V, no memory photo-response state in negative photocurrent. e, $V_g = 17$ V, off state. f, $V_g = 40$ V, no memory photo-response state in positive photocurrent.

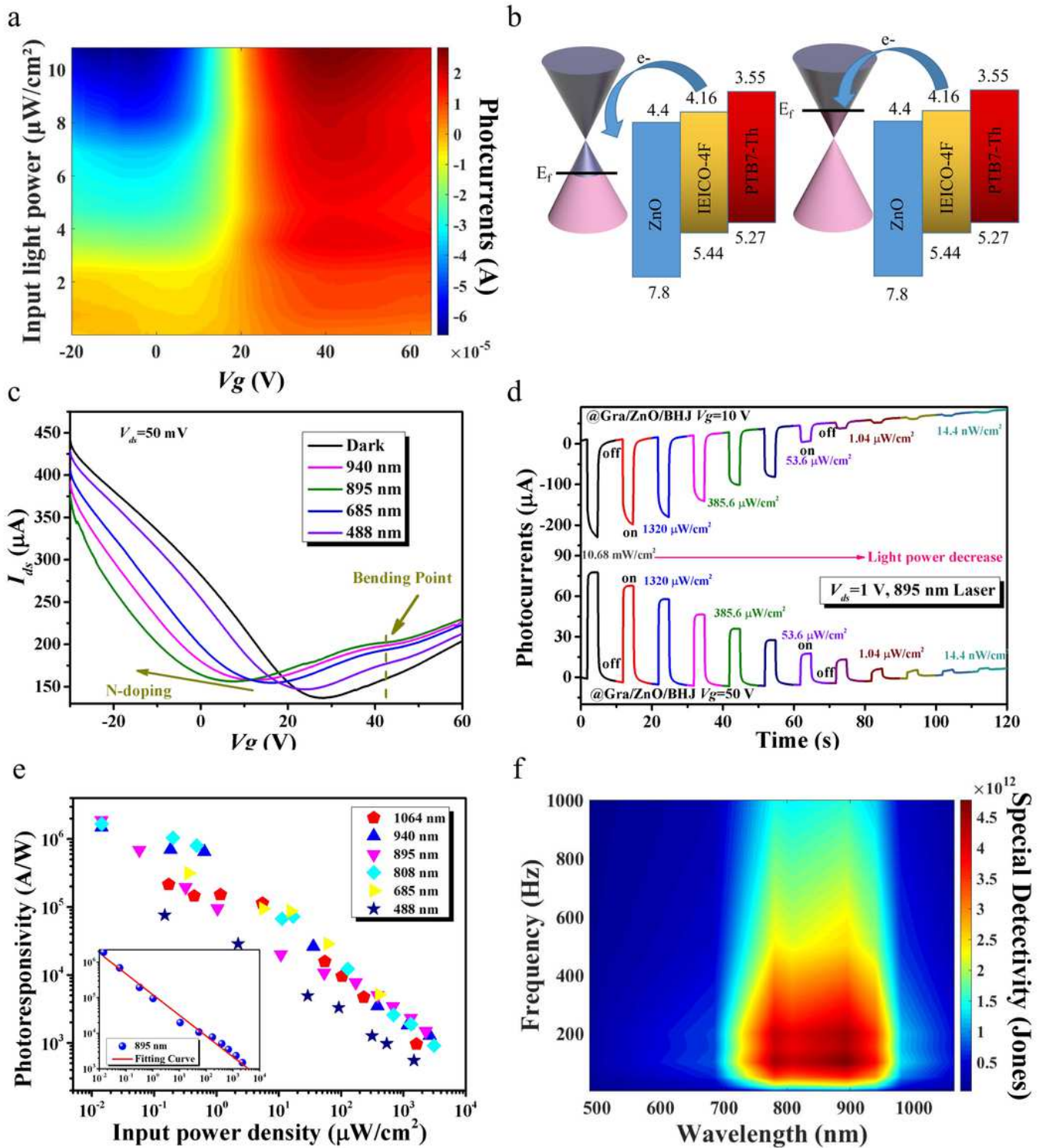


Figure 2

The transfer, no memory photo-responsive characteristics of graphene/organic phototransistor. a, V_g and Power dependent photocurrents intensity distribution colormap. b, The energy band alignment and charge transfer diagram of the multi-layer heterojunction under the light illumination at different V_g conditions. Top panel is deep-hole graphene circumstance and bottom panel corresponding to shallow-hole or electron branch graphene. c, Transfer characteristics of the graphene/organic phototransistor

under different input wavelengths with the same power density = 60 mW/cm². d, The photocurrent variations of the different V_g values ($V_g=10$ V top panel, $V_g=50$ V bottom panel) with the reductive input light power. e, The photo-responsivity plotted as a function of input light power density. The inside is the logarithm linear fitting curve. f, The frequency and wavelength dependent color map of detectivity.

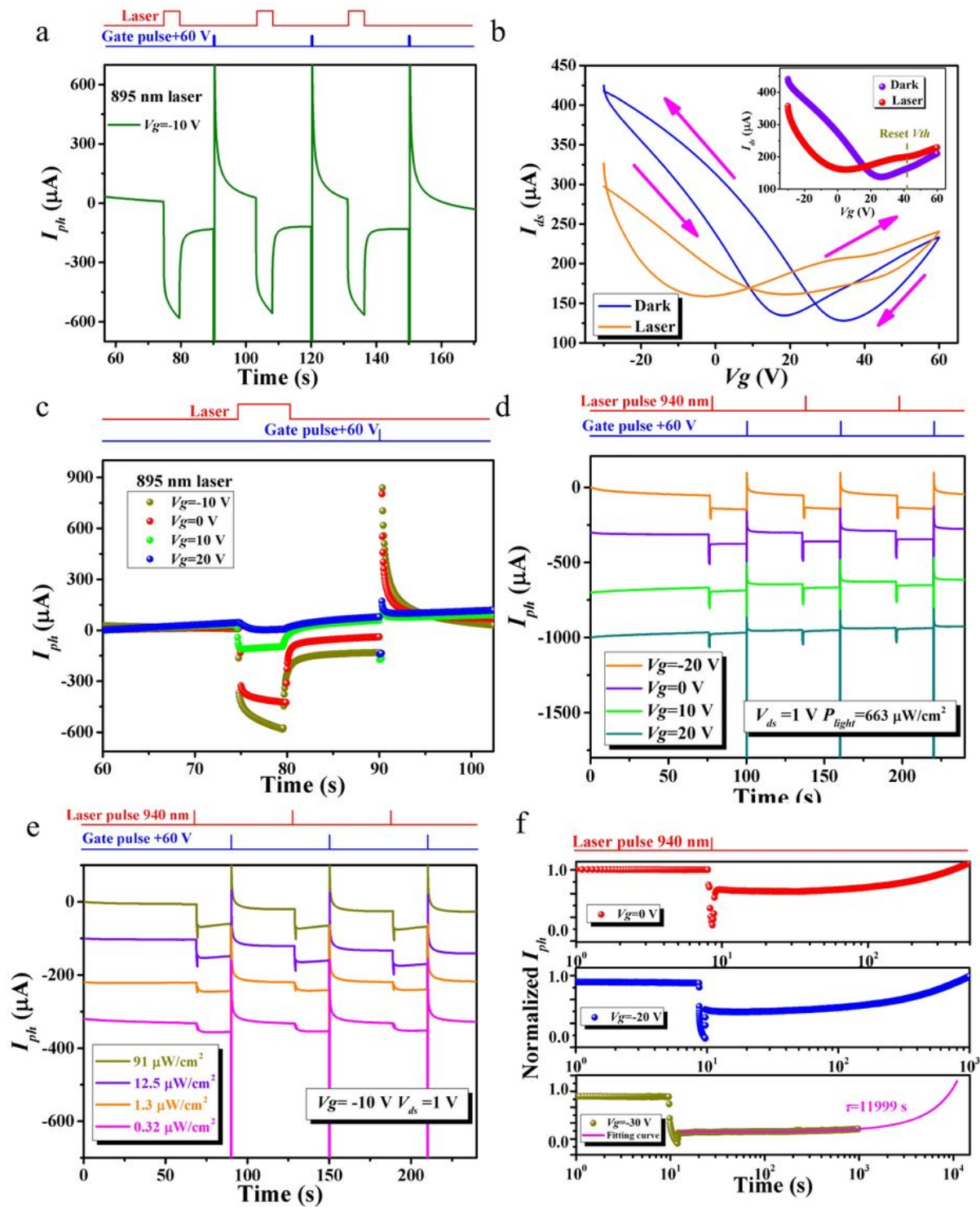


Figure 3

The transfer, infrared photo-memory cycle and retention characteristics of graphene/organic phototransistor. a, The 3 writing and erasing cycles. b, The hysteresis transfer curve along with arrow direction and inside is transfer curve of device with or without light illumination. c, The gate-dependent photo-memory switching operation. d, Gate-related relaxation currents under the constant input light power with 1 s pulse width. For all traces, input light power=663 $\mu\text{W}/\text{cm}^2$, gate pulse width=0.25 s. e, The 3 programming-relaxation cycle measurements as the function of input light power. light pulse width=0.5 s, gate pulse width=0.25 s. f, The retention and persistent state of infrared photo-memory with different V_g (two of top panel). Optimized retention in bottom panel with proper input power and V_g .

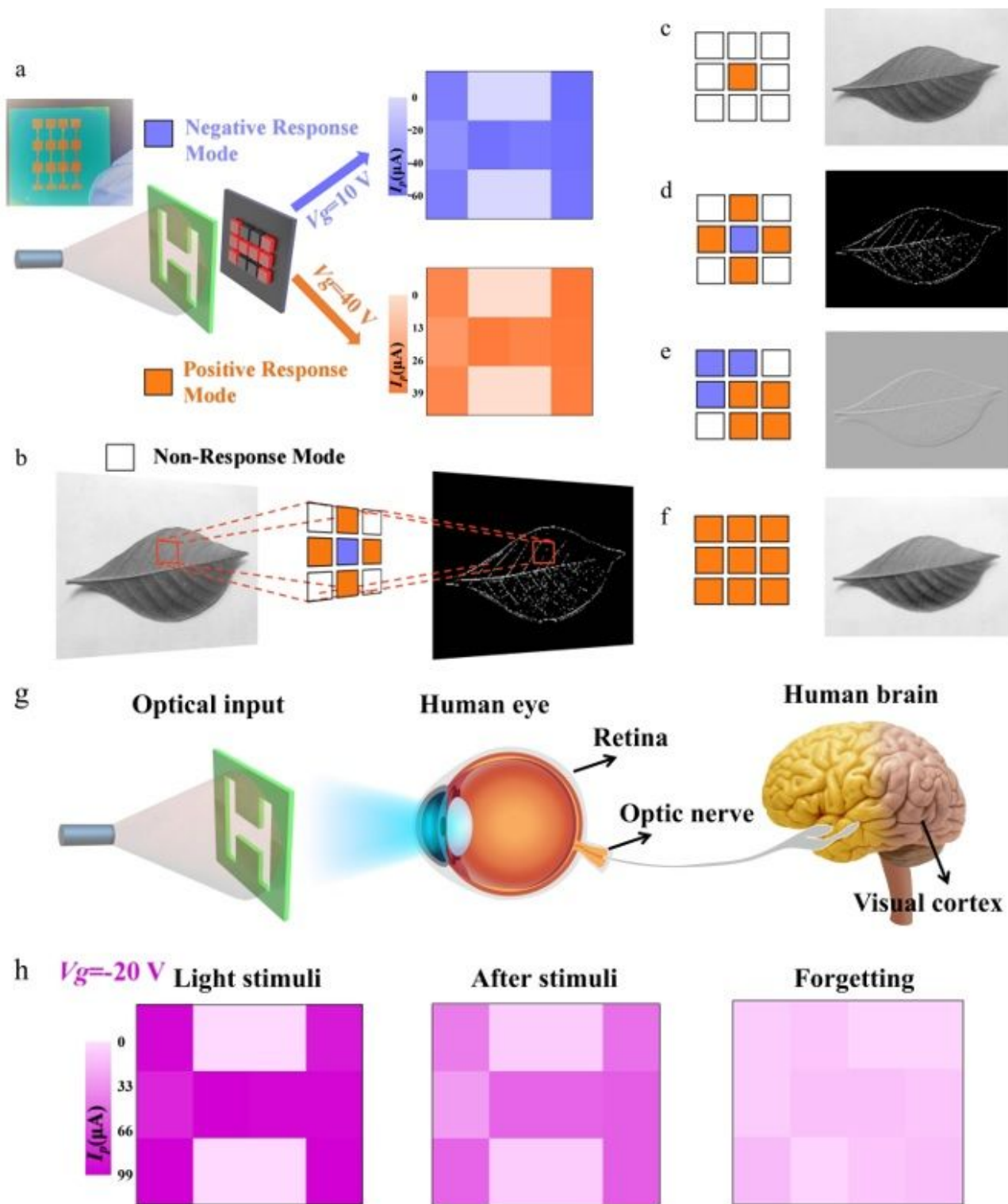


Figure 4

The planar array of graphene/organic phototransistors for reconfigurable retinomorph vision and memorial preprocessing application. a, The schematic diagram of 3×4 array irradiated by infrared light irradiation metal through the shadow mask with ‘H’ shaped pattern and photoresponse of the negative and positive photoresponsive modes with the infrared 940 nm light (3.76 mW/cm²) for imaging. Inset is the 3×4 array picture. b, Simulations of reconfigurable retinomorph vision. c, Original image. d, Edge

detection. e, Emboss. f, Dispose of Blurring. g, Schematics of the human visual system. h, The illustrations of the image memory of the letter 'H' at memorial preprocessing working mode ($V_g = -20$ V, 940 nm light with 3.76 mW/cm², optical pulse width: 2s, electric pulse width: 1s).

Supplementary Files

This is a list of supplementary files associated with this preprint. Click to download.

- [supportinginformation.docx](#)